7. Scramjet-based measurements

Calibration experiments, while necessary, do not test how a diagnostic will perform in a shock tunnel measurement. Measurement of temperature and water vapour in a scramjet combustor was the primary focus of this work and this chapter describes the results obtained during scramjet-based measurements.

Descriptions of the shock tunnel and the scramjet have been given earlier in chapter 3, so these are not dealt with again. Similarly, the design and operation of the diode laser sensor has been described in chapter 5 so, in section 7.1, only additions to the sensor which were required for integration with the scramjet are described. In addition, section 7.1 reviews the operation conditions for the test.

Raw absorbance data from a representative tunnel run are presented in section 7.2. These data were obtained with the log–ratio detector and were affected by luminosity. To determine the extent of this effect, a direct measure of luminosity from a linear detector is presented next.

In section 7.4, line fits to absorption data at a variety of conditions are shown along with time series showing how absorbance changes over tunnel runs. Absorbance is then converted into temperature and concentration time-series, which are examined for repeatability in section 7.5. Temperature and concentration is then averaged over part of the tunnel run and plotted for different heights in the duct. Finally, time-series taken with ethylene fuel are shown and compared with those obtained when fueling the combustor with hydrogen.

7.1 Test outline and sensor configuration

A wide parameter space is available for investigation, variables include the location of the beam in the duct, operation conditions of the tunnel, fuel injection rates and fuel types. In order to limit this to something manageable, as well as maximise the chance of obtaining useful data from the diode laser sensor, the following approach was taken:

- Tunnel operation conditions were held constant, with values given in section 3.1, to correspond with work done by others [75] on a similar scramjet geometry;
- Two equivalence ratios were tested, a ‘low’ case with Ludwieg tube fill pressure of 950 kPa and a ‘high’ case with Ludwieg tube fill pressure of 2500 kPa, further details were provided in section 3.2;

- Position within the duct was varied along a vertical traverse, but a reference location was chosen 10.6 mm above the duct floor for testing repeatability;
- Absorption was generally measured with a log–ratio detector. Measurements were also made with a linear detector to investigate the contribution of luminosity and for comparison with results obtained with the log–ratio detector; and
- The combustor was fueled with hydrogen, except for two runs of the tunnel which used ethylene to verify the operation of the sensor in an ethylene-fueled environment.

Compared with flame measurements, experiments in the scramjet required more consideration to be given to how the probe beam would be introduced to the measurement location. The scramjet model was mounted inside a vacuum-sealed shock tunnel test section, without direct optical access. Access to awkward locations, however, is one of the major technical benefits of diode laser-based spectroscopy.

In general, two methods can be employed. One option is to use fibre-optics to transmit the laser output to the test location, which means that the laser system can be built from off-the-shelf components. Alternatively, the system can be miniaturised and built into the scramjet model, which can result in a system that doesn't need optical fibre.

Both approaches have their relative advantages and disadvantages, and refinement of a sensor may see a change between the two methods. For a system that needed to be dropped 27 m and withstand deceleration loads of 100 g, Silver, Kane and Greenberg's first generation sensor [106] used fibre-optics to transmit laser light in both directions between the top of the drop tower to the falling test rig. In their next refinement of their sensor [105], the electronics were built into the test rig which required better integration but did not require fibre-coupling.

For this work, light was coupled into fibre-optics which meant that:

- Less time was required for the mechanical design of the diode laser system;
- Only small changes, unplugging and plugging in connectorised fibre optics, were required to switch between flame and tunnel measurements;
- There was convenient access to the laser and optical system for diagnostics and fine tuning; and
- The majority of the optical components were away from the dirty and harsh environment inside the tunnel test section.

The use of fibre optics can increase the cost of the system when compared with using bulk optics. Fibre is also wavelength-specific which limits the possible wavelengths that can be used, as well as making it difficult to change the system to a new operating wavelength.

If the entire system had been built inside the tunnel, more care would have been required for protecting the diode laser system from the environment and access to the lasers would have been restricted. Because a log–ratio detector was used, requiring the input of both signal and reference channels, the optical system would have been more complex than if a simpler detection scheme was used. It would have been impractical to build an interferometer inside the tunnel, so wavelength scanning would not have been measured for each run. Without an interferometer built into the sensor, the wavelength scanning behaviour of the lasers could be measured before installation but, as the scanning range is dependent on the details of the laser drive current, such an approach would have limited the flexability of the system.

The laser system was arranged on an optical table outside the shock tunnel and light was transmitted to the scramjet through single-channel, receptacle-style Oz Optics fibre-optic vacuum feed-throughs. The beam was then collimated by a Newport fibre-pigtailed gradient index, or GRIN, lens (F-COL-9-13). This collimator directed a $0.5\,\mathrm{mm}$ diameter beam through a wedged BK7 window (Oriel/Newport, 0.5° wedge, diameter of $12.7\,\mathrm{mm}$) and into the scramjet duct as shown in figure 7.1. Wedged windows were used to avoid étalon effects, in preference to anti-reflection coatings which may have been degraded after exposure to the flow.

On the far side of the duct, shown in figure 7.2, the beam passed through a similar window and then an optical interference filter (Thorlabs FB-1400-12 with $12\,\mathrm{nm}$ FWHM bandpass) to exclude flow luminosity. The centre wavelength of the passband of interference filters is dependent on the incident angle of the transmitted light, and decreases as the incoming beam moves away from normal incidence. This filter was tilted at 14° to shift the centre of the passband from the specified $1400\,\mathrm{nm}$ to around $1392\,\mathrm{nm}$, where the lasers were operating. The optimum angle was found experimentally by maximising laser transmission in a bench-top test.

The beam then illuminated the 'signal' photodiode on a log–ratio detector. An alternative would have been to couple the beam back into a fibre optic and transmit the signal back outside the shock tunnel. Power transmission into single mode fibre optics, however, is extremely sensitive to alignment, and others have generally found better results by directly illuminating the detector photodiode [3] due to beam steering effects in flows with density gradients.

Nevertheless, some applications have coupled light back into fibres such as the first sensor developed by Silver, Kane and Greenberg [105]. In contrast with the detection scheme used here, their sensor used wavelength modulation spectroscopy which is better at rejecting noise introduced by beam steering [123], and the measurement was in a less turbulent environment than the supersonic combustor studied in this project.

Some initial runs with this configuration showed that stray light was overwhelming the diode laser signal. The stray light was determined to be coming from outside the scramjet duct and was eliminated by winding optical blackout tape around the detector circuit board supports and around the back of the detector circuit board.

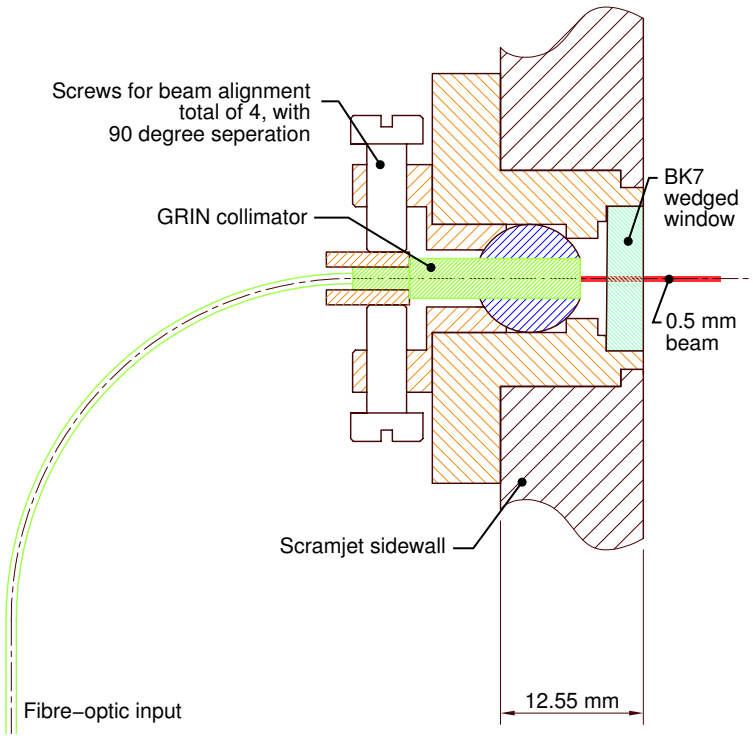

Figure 7.1: Cross-section of the fibre-optic launch module. Some of the fastenings have been excluded from the drawing for clarity. Co-designed with and built by Paul Walsh.

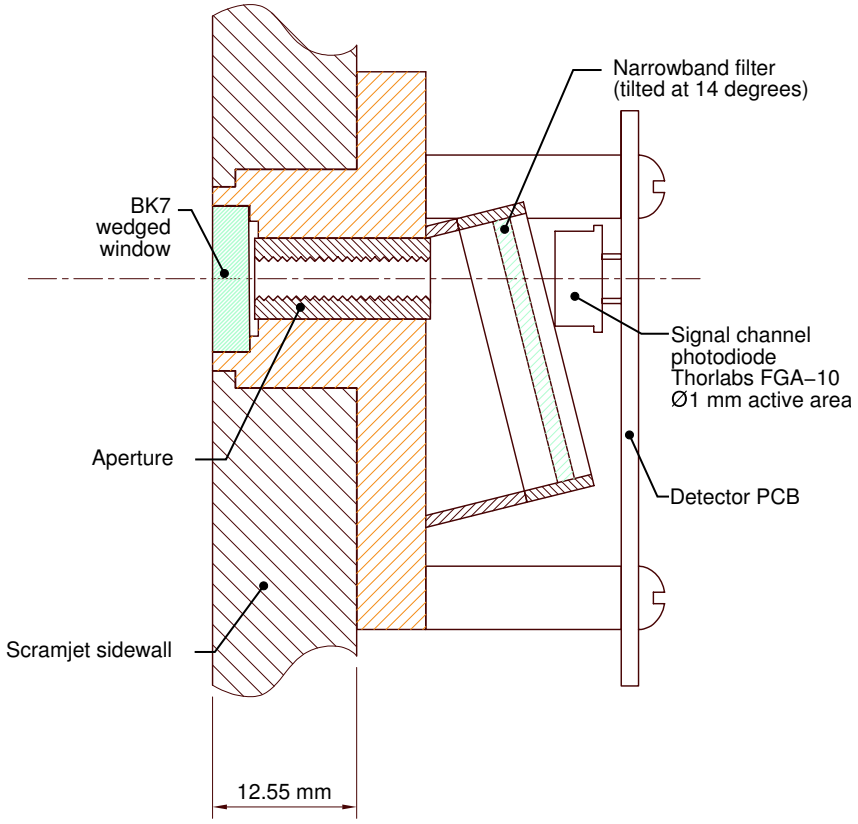

Figure 7.2: Cross-section of the detector module. Optical blackout tape is wound around the PCB supports and the rear of the PCB during operation to prevent stray light from contributing to the photodiode signal. Co-designed with and built by Paul Walsh.

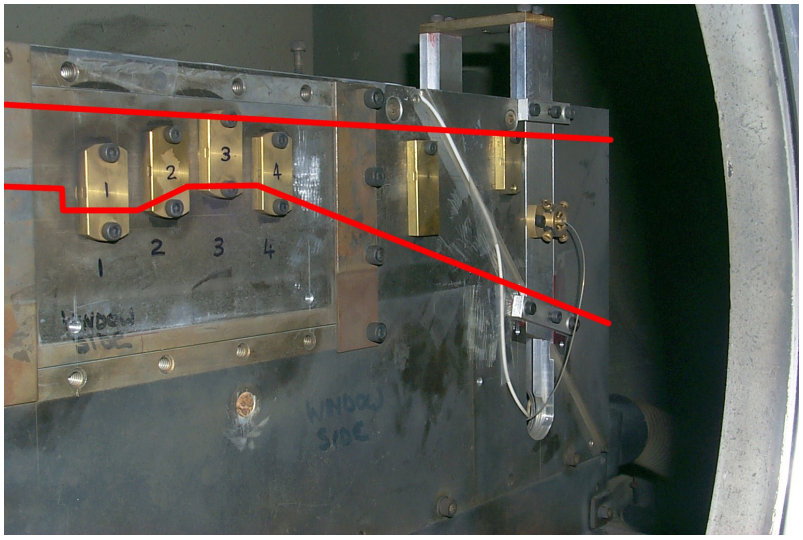

Figure 7.3: Photograph of the launcher module installed into the scramjet with the approximate location of the duct shown in red. A linkage between the launch and detector sides of the sliding section of the scramjet sidewall allow the laser alignment to be maintained as the measurement location is moved.

The optical and opto-electronic components were held in modules on either side of the duct. These modules could be removed easily and were located in a sliding section of the scramjet sidewall, photographed from the launcher side in figure 7.3, so that the beam could be located between 5.6 and 50.6 mm from the combustor floor. This covers around half of the vertical height of the duct, 97.6 mm at this point, and encompasses the region where the majority of water vapour was expected.

Before the shock tunnel was fired, covers were fitted over the modules to protect the optical components from the flow. The scramjet with covers in place is shown in figure 7.4.

7.2 Absorbance before processing

Unprocessed absorbance signal from the log–ratio detector is shown in figure 7.5. This is from a high equivalence ratio run, i.e. Ludwieg tube fill pressure of 2500 kPa, with the probe beam located 10.6 mm above the duct floor. In the first half of each scan one of the lasers crosses the line near 7179 cm^{-1}, designated as line 2. In the second half of each scan the other laser crosses the line near 7181 cm^{-1}, designated as line 1. Line 1 is visibly asymmetric due to the contribution of the additional high temperature line. Over the run time, line 1 becomes stronger relative to line 2, indicating a fall in temperature.

Spikes are evident in the data when the lasers switch on and off, at the start and in the middle of each scan. This noise does not contribute to the absorption measurement; its presence is actually useful to indicate that the maximum bandwidth of the detector and digitisation system is well above what is necessary to capture the absorption line shape.

Figure 7.4: Photograph of the scramjet with protective covers in place.

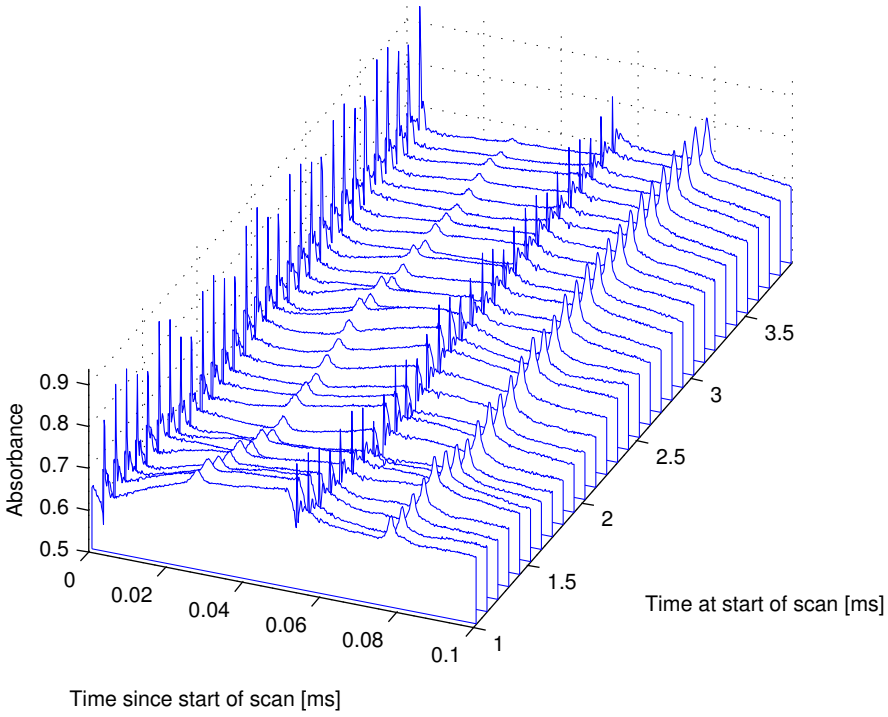

Figure 7.5: Absorbance during a high ϕ run with probe beam at 10.6 mm from the duct floor taken directly from log-ratio detector output without further processing. Line 1 is on the right of each scan.

The baseline absorption over each scan, as well as between scans, is not completely flat. The curve in the baseline, or a changing background absorbance with changing laser frequency, is characteristic of optical interference such as étalon fringes. For this system, the interference was tracked to passband ripple in the narrow-band filter.

While not visible in figure 7.5, other optical interference problems were also observed in the system. On occasion, when the beam was aligned with the detector, the alignment was sufficiently precise to form an étalon across the duct. When observed, this induced a peak-to-peak absorbance modulation of 0.02, but only required a very small de-alignment of the system to eliminate.

Another étalon formed in the system between the fibre-optic feedthrough and the termination of the signal channel optical fibre. While angled fibre connections were preferred for all parts of the system, component availability meant that these connections were flat polished. Since the length of fibre here was long, around 2 m, the étalon signal appeared at a very high frequency when compared with the laser scan rate. Since it was only within the detector bandwidth when the sensor was scanning at low frequency, it was initially mistaken an electronics problem. Once the signal was identified as optical interference, however, it was of no concern since it was outside the detector bandwidth when scanning at 10 kHz. Nevertheless, it emphasises the preference for angled connectors when using fibre in spectroscopy-based sensors. The presence of this étalon meant that the sensor, when installed in the shock tunnel, could not be operated below around 1 kHz. This would have been far too slow to acquire data from the shock tunnel.

Other sources of background interference are flow luminosity and beam steering from density gradients in the flow. Flow luminosity decreases both the mean value of absorbance over a scan and the peak height relative to baseline. Beam steering changes the overlap of the beam with the detector, causing fluctuations in the detected intensity as gas of different density is advected across the beam path. Furthermore, since the centre of the band-pass of the interference filter depends on the angle of incidence, beam steering interacts with the interference filter. If the passband ripple of the filter is thought of as a sinusoid waveform, changing the angle between the filter and the beam changes the phase of this sinusoid. This effect is evident in the results shown in figure 7.5 as the background in the first half of each scan changes from a curve which increases over each scan, for scans that begin near 1 ms, to be nearly flat in the last of the scans shown.

Flow luminosity does not appear to influence this data much, maybe being responsible for a decrease in the mean absorbance over scans starting near 2 ms. With the presence of beam steering and passband ripple, luminosity is difficult to estimate from this data. To better characterise the contribution of luminosity, some experiments were performed using a standard detector and a different analysis strategy.

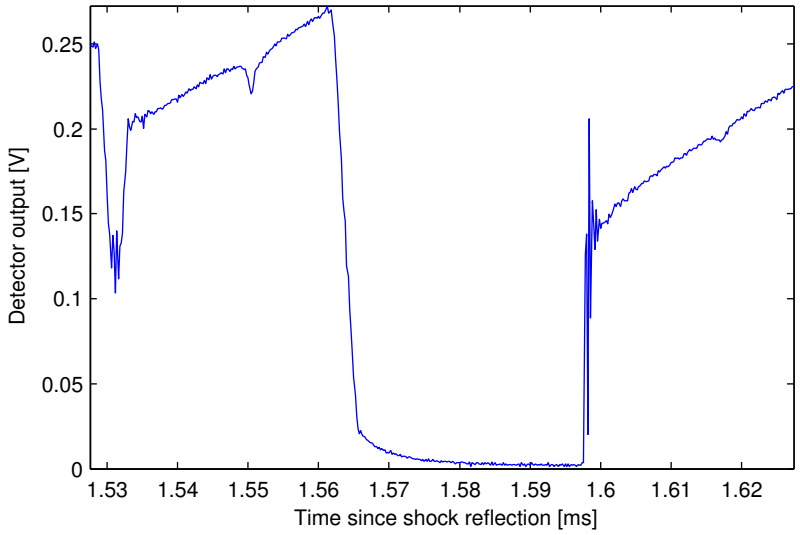

Figure 7.6: Raw signal from using a standard detector instead of the log–ratio detector during a high equivalence ratio test. Line 1 is scanned first, both lasers are switched off to record background luminosity and then the second laser scans across line 2.

7.3 Luminosity check

The use of the log–ratio detector helps to reduce noise and provides a signal that is simple to convert to absorbance. However electronic processing has the potential to hide certain features of the data. In particular, the log–ratio detector only provides an indirect measure of flow luminosity.

Broadband luminosity is present in the flow due to combustion as well as emission produced by the shock tunnel operation, mostly due to impurities in the flow [85]. Although laser output is spectrally narrow, the detector is sensitive over a wide wavelength range so that luminosity can be a problem if it is not considered in the sensor design.

In order to determine the importance of luminosity to the results shown above, the log–ratio detector was replaced with a standard photodiode detector—the low-noise design given by Gray *et al.* [47]—which was tested for linearity against a commercial power meter (Newport 840-C). The scan rate was reduced from 10 kHz to 5 kHz for this test and the scan broken into three segments: laser 1 on, laser 2 on and both lasers off. The signal, shown in figure 7.6, was then analysed following the procedure given in section 5.4 on page 63.

The luminosity signal was extracted from the portion of the scan where both lasers were turned off and then plotted as a ratio of the laser signal in figure 7.7. These results show that the luminosity contributes, at most, 1.5% to the detected signal. By modelling the luminosity as described in section 7.1 on page 99, curve fits to synthetic data show that the systematic error in the integrated absorbance introduced by ignoring the contribution of luminosity also turns out to be around 1.5%. If the two lasers are operated at similar power, this error cancels out in the determination of the line ratio, R_{ls}. Therefore,

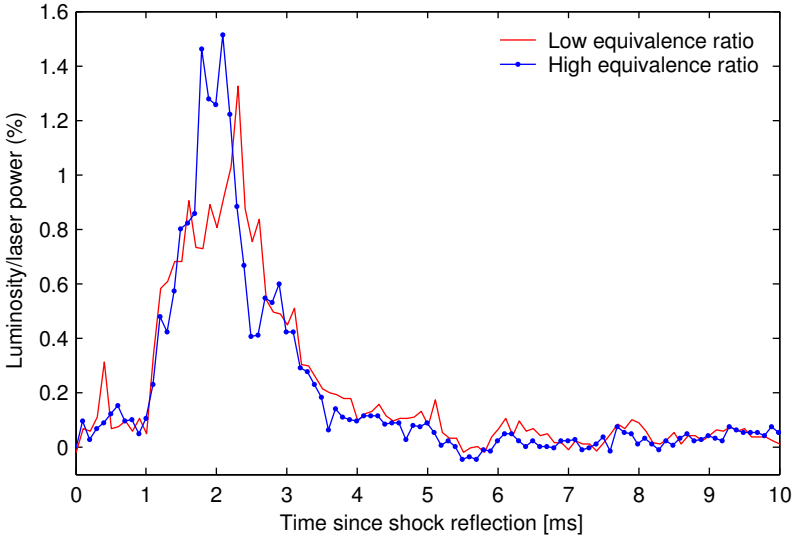

Figure 7.7: Flow luminosity expressed as a percentage of laser power for direct-absorption experiments.

the temperature measurement is unaffected by ignoring luminosity and water vapour concentration is underestimated slightly if luminosity is ignored. As it was small, this systematic error was accepted and lines were fit to absorption data without applying a correction for luminosity.

While the signal-to-noise ratio was worse for the direct-absorption measurements, the results were consistent with the results obtained with the log–ratio detector.

7.4 Integrated absorbance

Having established that the effect of luminosity could be neglected during analysis, absorbance was determined from log–ratio detector ouput and Voigt line profiles fit to these data. Profiles were first fit to absorbance averaged for all of the scans taken over the run time and then the result of this fit was used as an initial guess for each individual scan. This approach provided a good initial guess for each individual scan, speeding up the processing and reducing the chance of fitting a line shape to noise.

The quality of line fits varied considerably due to the wide variety of flow conditions over each shot and in different parts of the duct. Locations where temperatures was near 800 K, where both absorption lines are relatively strong, and water vapour concentration was high provided the highest absorption signal and correspondingly best fits. These conditions were best met near the bottom of the duct at the high equivalence ratio.

Examples of fits to several single-scan line shapes are shown in figures 7.8 and 7.9. Figure 7.8 shows data acquired at the high equivalence ratio, 10.6 mm from the floor of the duct, while figure 7.9 shows data acquired at the low equivalence

ratio in the same location. Absorbance for the high equivalence ratio is double what is observed for the low equivalence ratio case.

The magnitude of the residuals in figures 7.8 and 7.9 are similar for all of the fitted data. This indicates that variation in the signal-to-noise ratio is dominated by the changing absorption signal, and this is highest at 2.5 ms in the high equivalence ratio case.

The residuals seem unrelated to whether or not the laser is scanning through an absorption line. This is in contrast with the residuals observed during test cell measurements, shown in figure 6.2 on page 80, where the largest residuals were observed as the laser scanned across the absorption line. The magnitude of the residuals in scramjet measurements, therefore, was primarily due to effects which are not frequency-dependent such as beam steering and background luminosity fluctuations; not fluctuations in absorbance from turbulent temperature and concentration variation.

Also visible in the line fits is the changing influence of the weak line, which appears near line 1. This is at its strongest, compared with line 1, in figure 7.8(a) which corresponds to the highest temperature out of these cases. The increasing influence of this line has the potential to degrade the fit at high temperature, since the quality of the fit of the main absorption becomes more dependant on how well the weaker overlapping line is fit.

As was described in section 5.4, the uncertainty in the fit parameters can be estimated by the bootstrap Monte-Carlo method. This was used to provide an estimate of the 90% confidence interval for integrated absorbance for each curve fit. The integrated absorbance, with uncertainty, is shown as a function of time in figures 7.10 and 7.11 for high and low equivalence ratio cases respectively. This data is from the same two shots as the line shape data presented above and shows the changing absorbance due to the two spectral lines over the runs.

In each of the cases, unsettled conditions preclude line fits before around 1 ms, but conditions settle rapidly after this. Much more absorption is observed in the high equivalence ratio case, which provides lower relative uncertainty than the low equivalence ratio case. After around 3 ms, first for the low equivalence ratio case and then for the high equivalence ratio case, absorbance decreases for both spectral lines and line 2 becomes too weak to measure slightly after 4 ms.

Mean relative uncertainty between 1 and 3 ms at the high equivalence ratio is 4.4 % for line 1, 5.3 % for line 2 and, at the low equivalence ratio, 7.5 % for line 1 and 6.7 % for line 2. Uncertainty is controlled mostly by the line strength, so that the stronger line generally exhibits the lower relative uncertainty. However, line 1 exhibits more uncertainty than line 2 at times where both lines are of similar strength. This reflects the increased uncertainty in the fit caused by the line that overlaps line 1, since this fit requires more free parameters.

Generally, the uncertainty in the fits is smaller than the scatter in the data. This has the implication that, despite the smoothing effect of the line-of-sight integration, the fluctuations in the flow are larger than the measurement uncertainty. The fluctuations are largest in the low equivalence ratio case, despite uncertainty being similar. This analysis does not, however, indicate the level

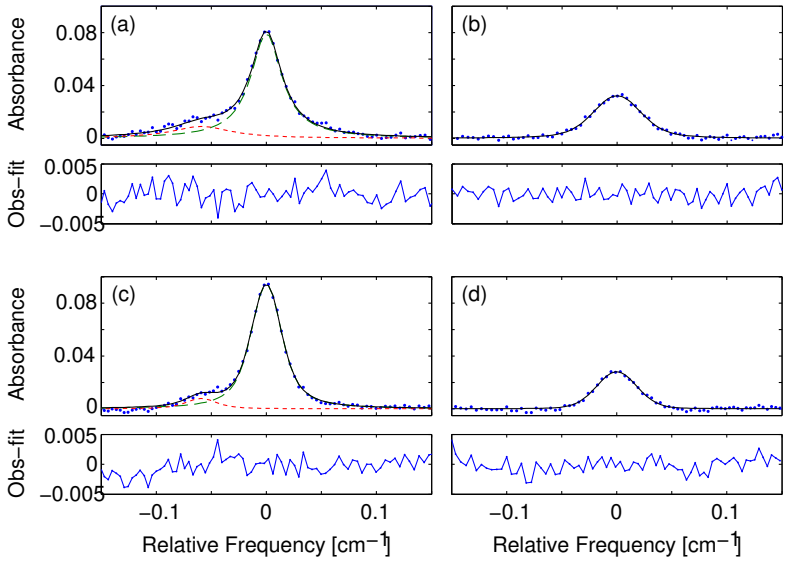

Figure 7.8: Curve fits to high equivalence ratio data, 10.6 mm above combustor floor: (a) shows line 1 at 1.5 ms, (b) shows line 2 at 1.5 ms, (c) shows line 1 at 2.5 ms and (d) shows line 2 at 2.5 ms. Data is shown as dots, the fit is shown as a solid line. Line 1 requires two Voigt profiles to be fit to the data, and these are shown as dashed lines. 'Obs-fit' means 'Observed−fitted absorbance', equivalently, the unnormalised residuals.

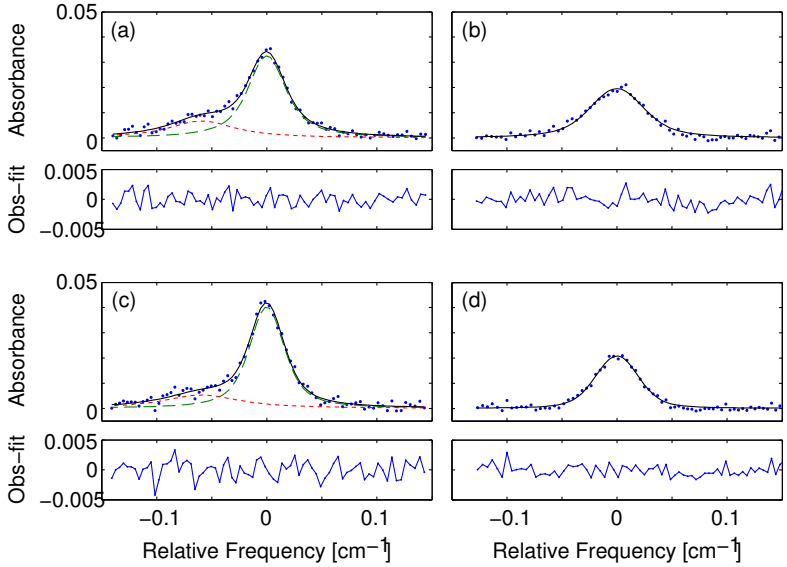

Figure 7.9: Curve fits to low equivalence ratio data where the panels have the same meaning as figure 7.8. Absorbance is scaled between 0 and 0.05, half the range of figure 7.8.

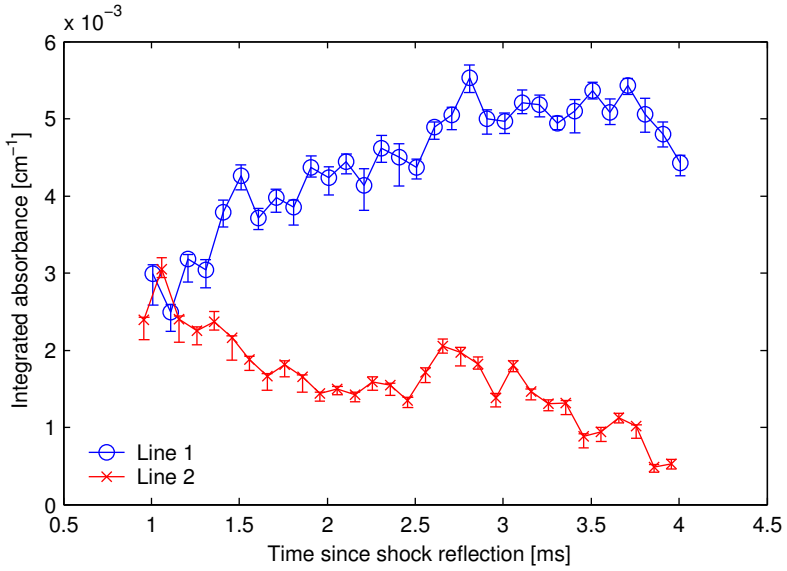

Figure 7.10: Integrated absorbance from 1 to 4 ms, 10.6 mm above the combustor floor for a high equivalence ratio run. Error bars show the 90% confidence interval of the fit.

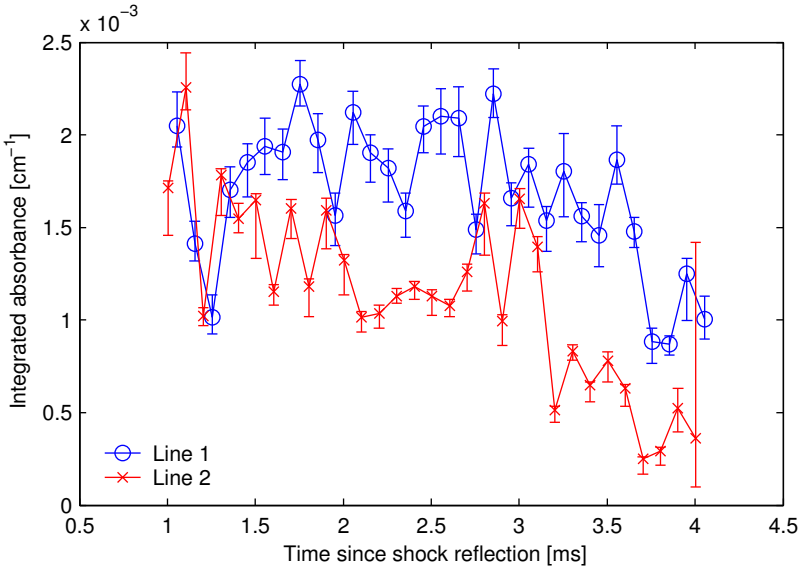

Figure 7.11: Similar to figure 7.10 but for the low equivalence ratio condition.

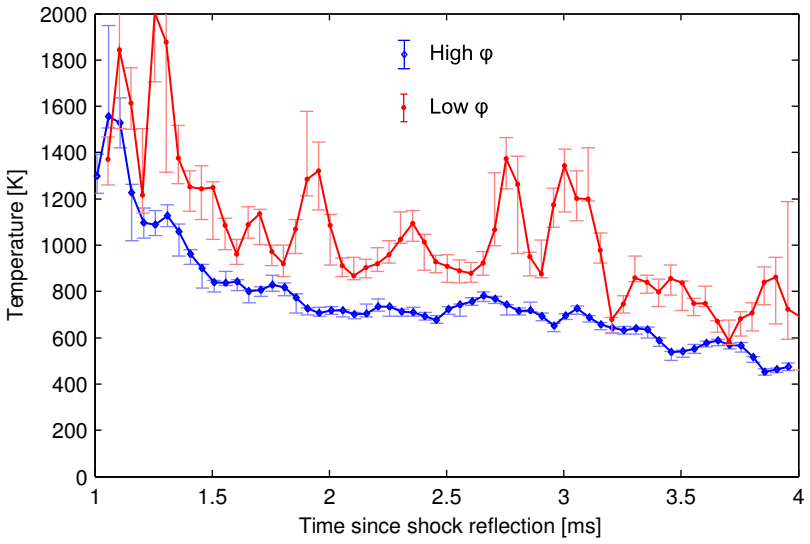

Figure 7.12: Line-of-sight temperature time-series for high and low equivalence ratio calculated from absorbance data in figures 7.10 and 7.11 with 90% confidence interval.

of fluctuations present on time scales smaller than the time required to scan across an absorption line, around 0.01 ms. Small time-scale variations in the flow are instead interpreted as a contribution to measurement noise by the present analysis.

Since the line strengths change relative to each other over the course of the run, it is apparent that temperature and water vapour number density changes over the run. This is better considered, however, after the absorbance data is converted to temperature and number density.

7.5 Temperature and water vapour time series

The procedure explained in section 5.4 was used to convert the absorbance data to temperature and water vapour concentration. Since the system is time-multiplexed, the two absorbance measurements are not made at precisely the same time and interpolation was used to calculate the line strength ratio R_{ls}. For each point that A_1 was measured at, A_2 was found by linear interpolation between the two closest points where A_2 was measured. A similar process was followed to obtain R_{ls} for each point where A_2 was defined with the result that R_{ls}, along with temperature and water vapour concentration, was obtained twice for each laser scan.

The analysis procedure also assumes constant properties along the beam line-of-sight since, unlike flame measurements, there was no other information about the spatial variation of properties along the beam path. Temperature calculated in this manner is shown in figure 7.12. This was calculated from the same data as above taken at 10.6 mm from the duct floor..

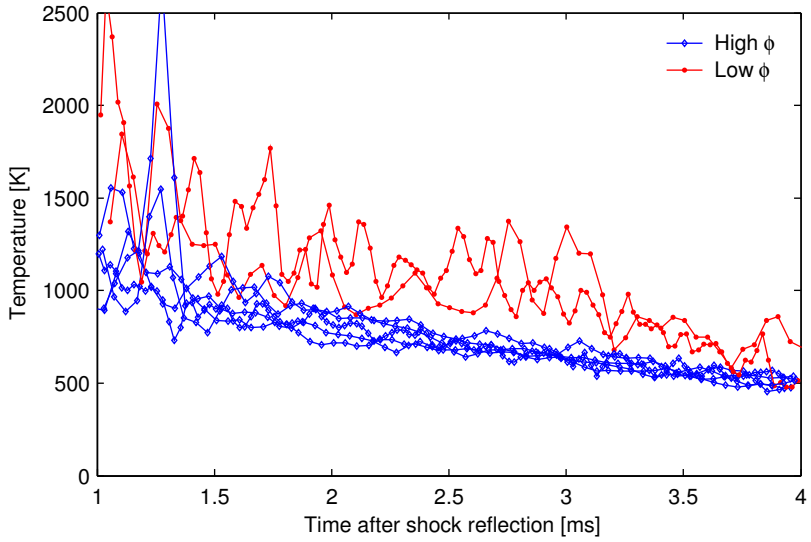

Figure 7.13: Temperature time-series for seven individual runs at two different conditions, 10.6 mm from the duct floor.

The repeatability of this result was tested over a total of seven shock tunnel runs, and produced the temperature and water vapour concentration results shown in figures 7.13 and 7.14 respectively.

Two of the cases shown in figures 7.13 and 7.14 show data taken at the low equivalence ratio while the other five are from the high equivalence ratio. Most of the runs were acquired at 10 kHz, however one of each of the high and low cases was acquired at 20 kHz.

The result is repeatable between the runs of the tunnel, and appears unaffected by the use of the higher sampling rate. Over all of the shots, for both high and low equivalence ratio, the temperature signal fluctuates about an approximately linear decrease. Water concentration, meanwhile, is relatively unchanged between 1 and 3 ms, especially in the low ϕ case, but decreases after 3 ms.

Temperature is higher in the low equivalence ratio case, 1100 K compared with 800 K at 2 ms, while water vapour concentration is around two-thirds of the high equivalence ratio case. The low equivalence ratio case also shows larger fluctuations in temperature and water vapour concentration, indicating larger fluctuations in the flow at this condition.

7.6 Traverse across duct

As well as data from 10.6 mm from the duct floor, several more shots were taken at the two equivalence ratios at different heights in the duct. Sufficient water vapour was present in the duct to obtain measurements up to 25.6 mm from the duct floor for the low equivalence ratio and up to 40.6 mm from the duct floor for th high equivalence ratio.

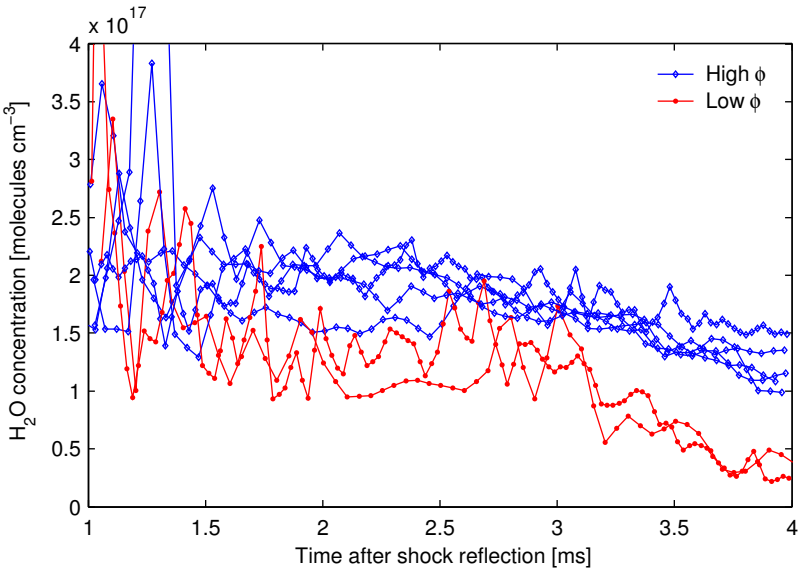

Figure 7.14: Number density for the same data as figure 7.13.

Temperature and concentration were obtained at 2 ms by regression-fitting a line to data between 1.5 and 2.5 ms and then evaluating the value of the line at 2 ms. This approach resulted in the same value as simply taking the mean over 1.5 to 2.5 ms, but meant that fluctuations could be represented in terms of their standard deviation about the fitted linear trend. Since 10 measurements contribute to each point, the uncertainty in the mean at each point is less than the standard deviation by a factor of around $\sqrt{10}$ if normal distributions can be assumed.

Temperature and standard deviation is shown in figure 7.15 for the two equivalence ratio cases. The maximum temperature of over 2000 K was observed for the low equivalence ratio case, 15 mm above the duct floor. This is the most uncertain of the measurements presented, with some of the points making up the fit reaching 3000 K, which is well outside the optimal range for this pair of transitions. Despite uncertainty in the temperature at this point, it is nevertheless the point where the highest temperature was observed, provided that the assumption of a homogeneous beam path is just as true as at the other measurement locations.

Either side of this maximum, the temperature for the low equivalence ratio case falls to more manageable temperatures, dropping off both towards the wall and towards the middle of the duct. Temperature for the high equivalence ratio case shows a similar decrease towards the duct floor but increases towards the centre of the duct, reaching a maximum at 30.6 mm from the floor and then showing a decrease at the topmost measurement location, 40.6 mm from the duct floor.

The low equivalence ratio data is limited to the lower part of the duct because of a lack of signal, presumably due to low water concentration, higher in the duct. Concentration across the duct is plotted in figure 7.16. These data show

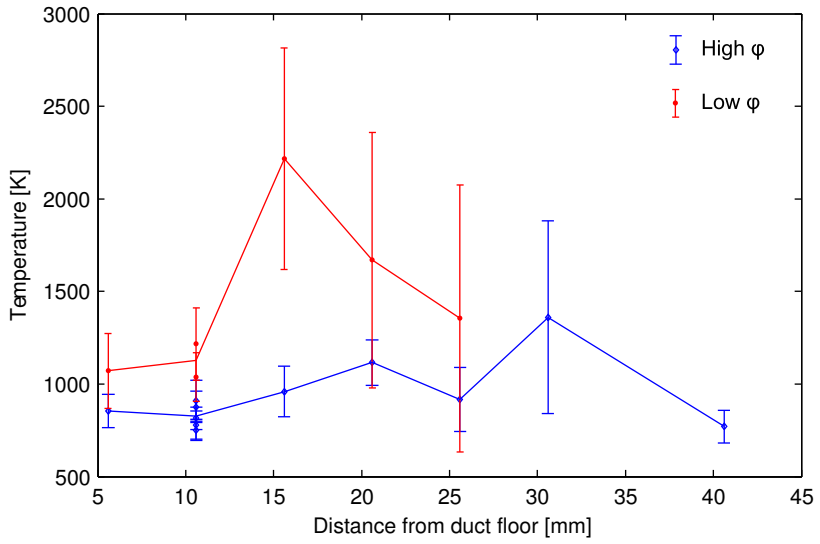

Figure 7.15: Temperature at 2 ms in different parts of the duct. Error bars indicate the standard deviation of temperature about a linear fit between 1.5 and 2.5 ms.

larger variability and poorer shot-to-shot repeatability than the temperature measurement, although trends are still visible in the data.

Compared with temperature, there is less delineation between the two cases. Water vapour concentration tends to decrease with increasing distance from the duct floor. The low equivalence ratio shows a peak at the same location as the peak in temperature. However, this point will be overestimated if the temperature is overestimated due to the dependence of water vapour concentration on temperature.

The high equivalence ratio case shows no significant peak in water vapour concentration, the highest concentration is located closest to the wall but is within the scatter of the other points. The sawtooth structure is also too small to necessarily be significant, especially when compared with the shot-to-shot scatter in the repeated measurement at 10.6 mm.

Better understanding of these results can be achieved through more consideration of the scramjet flow-field, and this will be tackled in the next chapter.

7.7 Measurements in ethylene-fueled combustor

Because of the importance of hydrocarbons as fuels in conventional jet engines, as well as the interest in using hydrocarbons for fueling scramjets [49], the present water vapour sensor was also used to gather data when fueling the combustor with ethylene instead of hydrogen.

Measurements were carried out at the same location used for most of the measurements, 10.6 mm above the scramjet floor, at two equivalence ratios. For the low equivalence ratio, the Ludwieg tube was filled with ethylene to 510 kPa and to 1450 kPa for the high equivalence ratio.

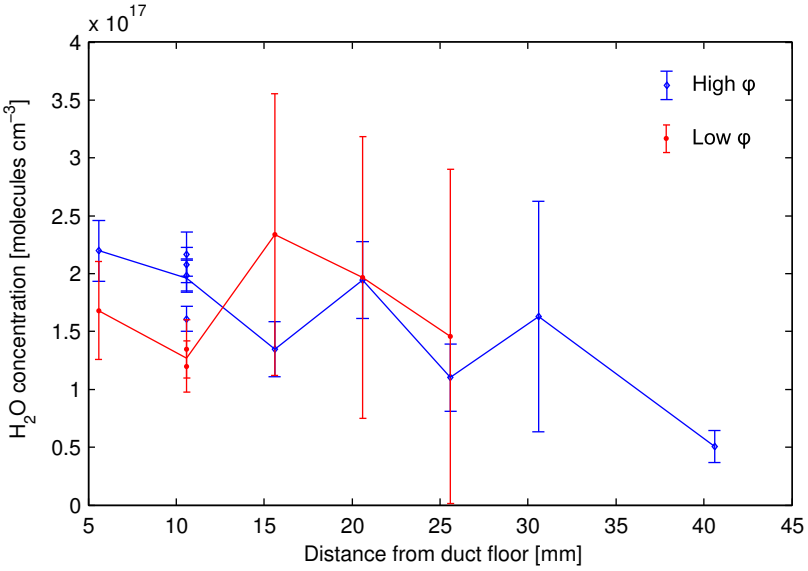

Figure 7.16: Water vapour concentration at 2 ms in different parts of the duct. Error bars indicate the standard deviation of temperature about a linear fit between 1.5 and 2.5 ms.

Since combustion products besides water were expected for ethylene, less water vapour was expected when compared with the hydrogen measurements. This turned out to be the case and, as a result, the temperature measurements shown in figure 7.17 have higher uncertainties than for the hydrogen cases. Low absorption makes measurements impossible sooner in the test, at around 3.5 ms instead of after 4 ms.

Similar trends to the hydrogen fueled cases are apparent, with the low equivalence ratio recording a higher temperature as well as temperature decreasing over the test time.

Concentration also follows similar trends to the hydrogen case, as shown in figure 7.18. Water vapour concentration is lower in the low equivalence ratio case although, for both the low and high equivalence ratio, there is around one quarter as much as in the hydrogen fueled cases.

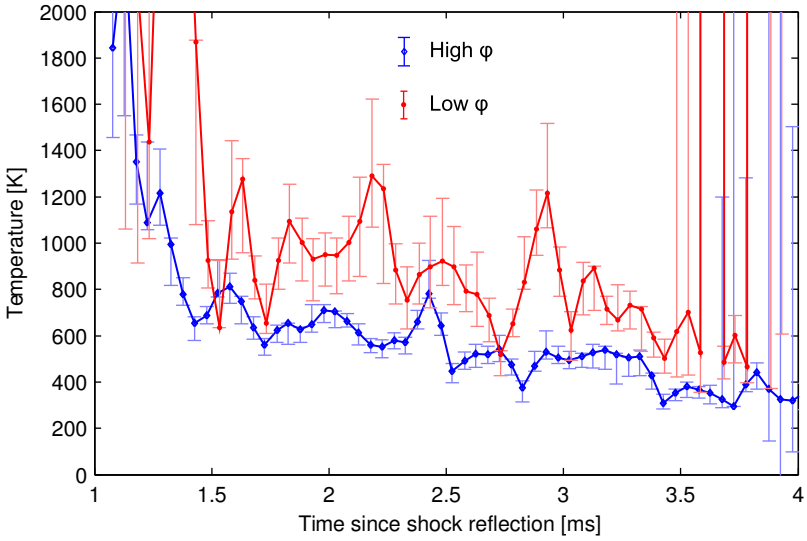

Figure 7.17: Temperature for an ethylene-fueled run. High equivalence ratio here means a fill pressure of 1450 kPa and low equivalence ratio means a fill pressure of 510 kPa.

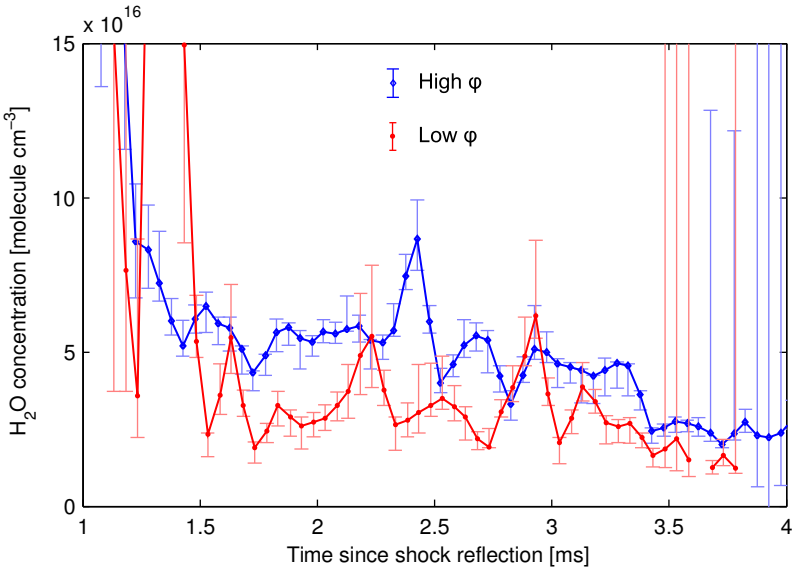

Figure 7.18: Water vapour concentration for an ethylene-fueled run. High equivalence ratio here means a fill pressure of 1450 kPa and low equivalence ratio means a fill pressure of 510 kPa.